Journal of Materiomics 12 (2026) 101326

Contents lists available at ScienceDirect

Journal of Materiomics

journal homepage: www.journals.elsevier.com/journal-of-materiomics/

High-entropy strategy for stabilizing oxygen redox in layered oxide cathodes for Na-ion batteries

Rongbin Dang [a], Rui Gao [e], Weiliang Xu [b], Xiaohui Rong [b,*], Dongdong Xiao [b], Feixiang Ding [b], Lin Zhou [b], Huican Mao [c,**], Yaxiang Lu [b], Junmei Zhao [d,***], Meicheng Li [a,****], Yong-Sheng Hu [b,*****]

[a] State Key Laboratory of Alternate Electrical Power System with Renewable Energy Sources, School of New Energy, North China Electric Power University, Beijing, 100096, China
[b] Beijing National Laboratory for Condensed Matter Physics, Institute of Physics, Chinese Academy of Sciences, Beijing, 100190, China
[c] Department of Materials Science, Key Laboratory of Automobile Materials, MOE and International Center of Future Science, Jilin University, Changchun, 130012, China
[d] CAS Key Laboratory of Green Process and Engineering, Institute of Process Engineering, Chinese Academy of Sciences, Beijing, 100190, China
[e] Institute for Clean Energy Technology, North China Electric Power University, Beijing, 102206, China

ARTICLE INFO

Article history:
Received 14 July 2026
Received in revised form
13 August 2026
Accepted 10 September 2026
Available online 23 September 2026

Keywords:
Na-ion battery
Cathode materials
Oxygen redox
High entropy
Long cycling

ABSTRACT

Activating oxygen redox (OR) reactions is an effective strategy for increasing the specific capacity and energy density of Na-ion batteries (NIBs). However, most OR cathodes require a high charge cut-off voltage (≥4.4 V), which severely compromises structural stability and accelerates electrolyte decomposition. In addition, practical cathode materials should possess high sodium content and robust structural stability to ensure high capacity and long cycle life. Herein, we propose a high-entropy O3-type layered oxide, $Na_{0.9}Li_{0.1}Mg_{0.1}Ni_{0.1}Cu_{0.1}Mn_{0.4}Ti_{0.2}O_2$ (HE-NLMNCMTO), as a practical oxygen-redox cathode. Benefiting from the elevated oxygen activity induced by the high-entropy configuration, oxygen redox can be fully activated at a relatively low cut-off voltage of ~4.2 V. Combined with the intrinsic structural stability of the high-entropy framework, HE-NLMNCMTO delivers a high reversible capacity of 167.1 mA·h/g through synergistic cationic and anionic redox reactions and exhibits outstanding cycling stability with 91.2% capacity retention after 400 cycles at 1 C. The remarkable structural stability is confirmed by *in-situ* XRD, nano-CT and STEM analyses. Moreover, cylindrical cells and anode-free single-layer pouch cells based on HE-NLMNCMTO exhibit excellent electrochemical performance, demonstrating its considerable potential for practical applications. This work provides a viable high-entropy strategy for developing durable and practical oxygen-redox cathodes for NIBs.
© 2026 The Authors. Published by Elsevier B.V. on behalf of The Chinese Ceramic Society. This is an open access article under the CC BY license (http://creativecommons.org/licenses/by/4.0/).

1. Introduction

Lithium-ion batteries (LIBs) have dominated the electrochemical energy storage market owing to their high energy density and excellent cycling performance, playing a pivotal role in the widespread deployment of portable electronics and electric vehicles [1,2]. However, the limited lithium resource and its uneven distribution cast a serious concern for its sustainable development. Consequently, Na-ion batteries (NIBs) have emerged as a promising alternative because of the natural abundance, low cost,

This article is part of a special issue entitled: Annual Meeting of CAST published in Journal of Materiomics.

* Corresponding author.
** Corresponding author.
*** Corresponding author.
**** Corresponding author.
***** Corresponding author.
E-mail addresses: rong@iphy.ac.cn (X. Rong), hcmao@jlu.edu.cn (H. Mao), jmzhao@ipe.ac.cn (J. Zhao), mcli@ncepu.edu.cn (M. Li), yshu@iphy.ac.cn (Y.-S. Hu).

https://doi.org/10.1016/j.jmat.2026.101326
2352-8478/© 2026 The Authors. Published by Elsevier B.V. on behalf of The Chinese Ceramic Society. This is an open access article under the CC BY license (http://creativecommons.org/licenses/by/4.0/).

and widespread availability of sodium resources [3–5]. Nevertheless, the relatively low energy density of NIBs remains a major obstacle to their practical application. This limitation primarily originates from the insufficient capacity of current cathode materials [6,7].

Layered transition metal oxides (Na_xTMO_2) are the most prevailing cathode hosts not only at the beginning but also nowadays [8]. Inspired by the high specific capacity of "Li-rich" compounds in LIBs, where additional capacity is achieved through anionic redox reactions [9,10], activating oxygen redox (OR) reactions in Na-based oxides opened up a new strategy to increase the energy density of NIBs. For instance, Rong et al. previously reported the P2-type $Na_{0.72}Li_{0.24}Mn_{0.76}O_2$ cathode for NIBs in 2019, which showed a high reversible specific capacity (~270 mA·h/g) and the highest energy density (~700 W·h/kg) between 1.5 V and 4.5 V [11]. Similarly, J–M Tarascon and co-workers proposed O3-type $NaLi_{1/3}Mn_{2/3}O_2$ synthesized through careful adjustment of synthesis conditions, which also displayed a reversible capacity of 190 mA·h/g contributed by OR and Mn^{3+}/Mn^{4+} redox processes.

Despite these advances, practical implementation of oxygen-redox cathodes remains challenging. Most reported materials require a high charge cut-off voltage (typically ≥4.4 V) to fully activate lattice oxygen, which accelerates irreversible phase transitions, oxygen release, electrolyte oxidation, and interfacial side reactions [12–15]. These issues inevitably result in rapid capacity fading, poor cycling stability, and limited practical applicability. Moreover, many P2-type oxygen-redox cathodes suffer from relatively low sodium content, restricting the amount of reversible Na^+ extraction/insertion and further limiting their achievable energy density. Therefore, an ideal oxygen-redox cathode for practical sodium-ion batteries should simultaneously satisfy several key requirements, including a moderate charge cut-off voltage, high sodium content, robust structural stability, and low material cost.

Recently, high-entropy oxides (HEOs) have attracted considerable attention because their entropy-stabilized structures often exhibit enhanced phase stability, suppressed structural degradation, and improved electrochemical performance [16,17]. Our previous research indicated that HEOs facilitate a more stable bulk structure and a more reversible phase-transition [18–20]. Fu et al. designed a high-configurational-entropy P2-type layered oxide $Na_{0.62}Mn_{0.67}Ni_{0.23}Cu_{0.05}Mg_{0.09-2y}Ti_yO_2$, which exhibited improved structural and thermal stability compared with conventional layered oxides [21]. These findings suggest that the high-entropy strategy provides an effective route to stabilizing layered oxide cathodes. However, its influence on oxygen-redox chemistry has not yet been systematically investigated.

Here, we report a high-entropy and cationic/anionic-redox O3-type layered oxide, $Na_{0.9}Li_{0.1}Mg_{0.1}Ni_{0.1}Cu_{0.1}Mn_{0.4}Ti_{0.2}O_2$ (HE-NLMNCMTO), as a practical oxygen-redox cathode for NIBs. The molar configurational entropy of these oxides can be calculated using Equation (1):

$$S_{\text{config}} = -R\left[\left(\sum_{i=1}^{N} x_i \ln x_i\right)_{\text{cation-site}} + \left(\sum_{j=1}^{N} x_j \ln x_j\right)_{\text{anion-site}}\right] \quad (1)$$

where x_i and x_j are the mole fractions of the elements at the cation and anion sites in the bulk structure, respectively. R is the universal gas constant. Because only one anion is present (*i.e.*, the possible oxygen vacancy is ignored), the minor effect of the anion site on Sconfig was not considered. The Sconfig of HE-NLMNCMTO is 1.7R, which is calculated via the above equation. Based on the configurational entropy introduced by Murty et al., "high entropy" is defined when the Sconfig≥1.5R [22]. So, the designed HE-NLMNCMTO can be classified as HEOs.

As expected, unlike conventional oxygen-redox cathodes, HE-NLMNCMTO enables complete oxygen-redox activation at a substantially reduced charge cut-off voltage of approximately 4.2 V. Density functional theory (DFT) calculations reveal that the high-entropy configuration elevates the oxygen 2p electronic states toward the Fermi level, thereby facilitating oxygen oxidation at lower potentials. Benefiting from the high Na content, this O3-type HE-NLMNCMTO displayed a high initial charge capacity of 195.8 mA·h/g and a reversible discharge capacity of 167.1 mA·h/g. More importantly, the entropy-stabilized structure effectively suppresses structural degradation during repeated cycling, resulting in an exceptional capacity retention of 91.2% after 400 cycles at 1 C, representing one of the best cycling performances reported for oxygen-redox cathodes. Finally, Furthermore, the reduced use of Ni and Li lowers the estimated bill of materials (BOM) cost. Kilogram-scale synthesis was successfully achieved, and both cylindrical full cells and anode-free pouch cells employing HE-NLMNCMTO demonstrated excellent electrochemical performance and long-term cycling stability. These results demonstrate that the high-entropy strategy not only stabilizes oxygen-redox chemistry but also provides a practical pathway toward high-energy, long-life sodium-ion batteries.

2. Experimental section

The detailed experimental section are provided in the Supporting Information.

3. Results and discussion

3.1. Theory calculations and performance comparisons

To further highlight the characteristics of the HE strategy for OR oxides, non-HE $Na_{0.9}Li_{0.2}Ni_{0.15}Mn_{0.65}O_2$ (non-HE-NLNMO) was purposely designed. Compared with HE-NLMNCMTO, non-HE-NLNMO has the same Na content and amount of TM, where 0.2Li triggers OR and 0.15 Ni^{2+} provides cationic charge compensation (0.3 e^- transfer), ensuring that differences in electrochemical behavior primarily originate from configurational entropy rather than compositional variations. The Sconfig of non-HE-NLNMO was 0.98R, significantly lower than that of HE-NLMNCMTO (1.7R). The refined oxygen occupancy from XRD and the homogeneous cation distribution from EDS confirm that oxygen vacancies, if any, are below the detection limit; thus, the anion-site entropy term is justifiably omitted. Firstly, we performed DFT calculations to optimize the structures of both HE and non-HE configurations across a range of Na contents from $Na_{0.9}$ to $Na_{0.3}$. As shown in Fig. S1–S13, the formation energies of HE-NLMNCMTO are consistently lower than those of non-HE-NLNMO at any given Na content, demonstrating the superior thermodynamic stability of the high-entropy phase.

To further reveal the electronic origin of the enhanced oxygen-redox behavior, the partial density of states (pDOS) of the initial and desodiated HE and non-HE structures were analyzed. As shown in Fig. 1a, the O pDOS below Fermi level (E_f) is more prominent for HE-NLMNCMTO than that of non-HE-NLNMO, indicating a greater charge distribution on oxygen atom in the HE configuration. When 0.3Na^+ was extracted for bulk structure (Fig. 1b), the O 2p states in HE-NLMNCMTO shift closer to the Fermi level and exhibit finite electronic states at E_f, suggesting that oxygen can participate in charge compensation at lower electrochemical potentials. The random distribution of six cations creates a wide distribution of

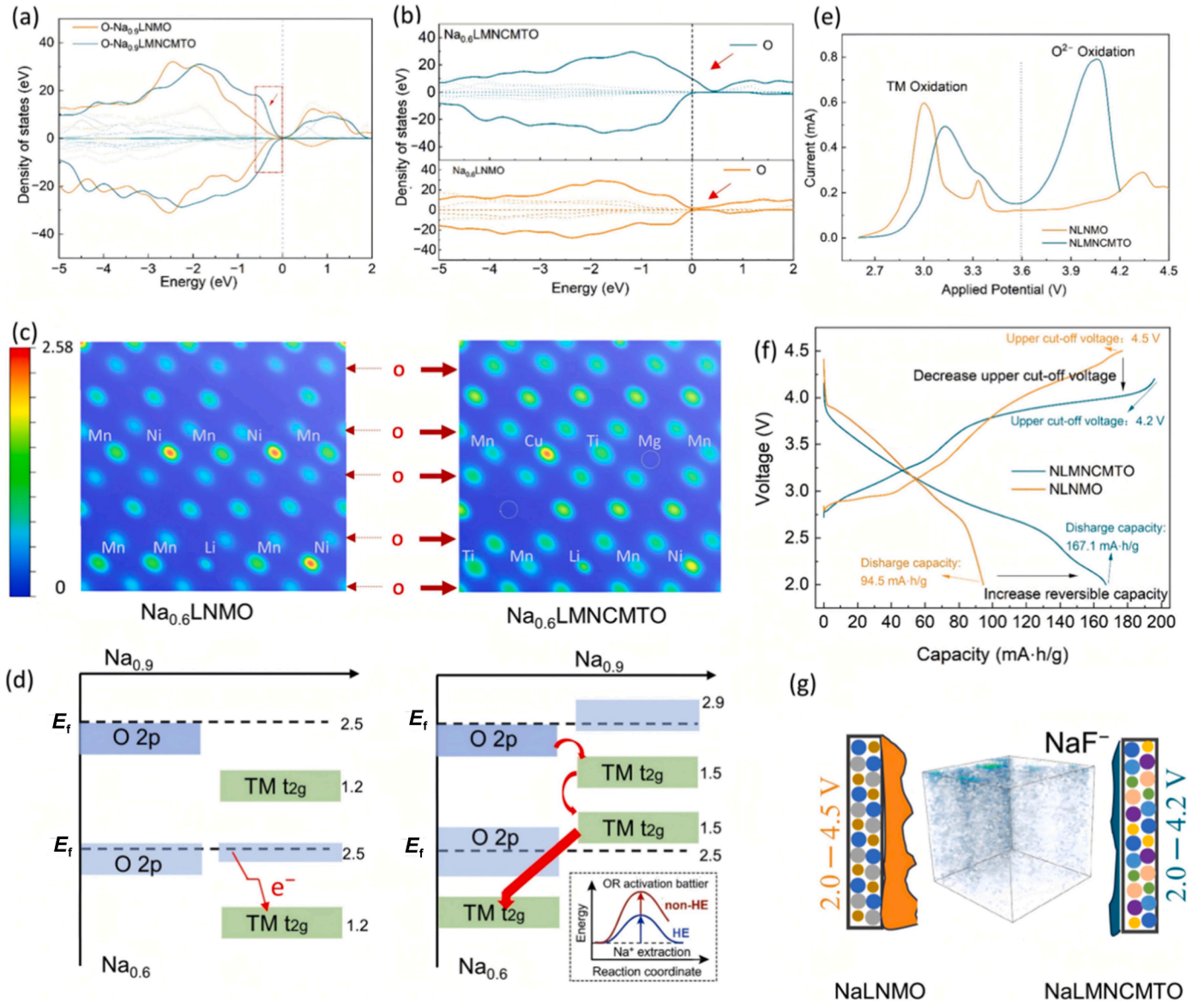


Fig. 1. Electronic origin and electrochemical characterization between HE and non-HE structures. O-pDOS and TM-pDOS (dotted line) for both HE-Na_xLMNCMTO and non-HE-Na_xLNMO at Na contents of (a) 0.9 and (b) 0.6; (c) Electron density nephogram of the O-TM-Na layer in the [102] direction for $Na_{0.6}$LNMO (left) and $Na_{0.6}$LMNCMTO (right). (d) Schematic electronic energy-level diagrams comparing the non-HE (left) and HE (right) configurations at two desodiation states, Na0.9 and Na0.6. The inset compares the activation energy barriers for oxygen redox (e–f) Experimental initial charge CV profile comparison and initial charge-discharge profiles of HE-NaLMNCMTO and non-HE-NaLNMO. (e) Comparison of HE-NaLMNCMTO and non-HE-NaLNMO as well as the 3D rendering of NaF- from TOF-SIMS characterization of HE-NaLMNCMTO after being charged and discharged for one cycle.

TM–O bond lengths, which broadens the O 2p band and raises its upper edge toward E_f. This electronic effect is the root cause of the lowered oxygen-redox potential, as corroborated by the increased O pDOS at E_f in the HE case. Fig. 1c presents the electron density (at isosurfaces of 0.3 e/Å^3) of the O–TM–O–Na layer viewed along the [102] direction for the electronic structures of both desodiated HE-$Na_{0.6}$LMNCMTO and non-HE-$Na_{0.6}$LNMO materials. Evidently, the electron density localized on the oxygen layer was higher in the HE configuration than that in non-HE configuration. The energy-level diagrams in Fig. 1d elucidate the electronic origin of the enhanced oxygen redox in the HE system. Unlike the non-HE case, where the O 2p band remains largely below E_f, the HE configuration causes a pronounced upward shift of the O 2p band towards E_f, particularly at $Na_{0.6}$. This shift facilitates electron transfer from oxygen to TM upon Na^+ extraction, thereby lowering the activation barrier for oxygen oxidation. As schematised in the inset, this reduced barrier rationalises the experimentally observed decrease in the OR onset potential from ~4.35 V (non-HE) to ~4.15 V (HE), confirming that high entropy promotes stable anionic redox at a more practical voltage. With further Na removal (Fig. S15), the density of states near E_f is demonstrated by the O character in both HE and non-HE cathodes, confirming that oxygen supplies the majority of the compensating electrons in this voltage regime. Overall, the HE cathode has a higher phase thermodynamic stability and more active OR activity. Therefore, a more stable and reversible OR reaction at a relatively low voltage can be expected for HE-NLMNCMTO.

The electrochemical behaviors of both OR cathodes of HE-NLMNCMTO and non-HE-NLNMO were subsequently verified. Fig. 1e shows the CV profiles of the initial charge process, which

reveals that HE-NLMNCMTO displays an intense oxidation peak corresponding to the oxidation of lattice oxygen at ~4.15 V, whereas the non-HE-NLNMO exhibits a smaller oxidation peak at a higher potential (~4.35 V). The initial charge-discharge profiles of both cathodes were shown in Fig. 1f. The non-HE-NLNMO display a initial charge capacity of 176.8 mA·h/g at an upper cut-off voltage of 4.5V. In contrast, HE-NLMNCMTO delivers a higher charge capacity of 195.8 mA·h/g at a increased upper cut-off voltage of 4.2V. More importantly, HE-NLMNCMTO could exhibit a higher reversible capacity of 167.1 mA·h/g compared with the only 94.5 mA·h/g of non-HE-NLNMO. Moreover, HE-NLMNCMTO also logically minimized the side reactions on the electrode surface, as demonstrated by the time-of-flight secondary ion mass spectrometry (TOF-SIMS) results shown in Fig. 1g and Fig. S16. So, the reduced charge cut-off voltage is highly compatible with currently available high-voltage electrolytes.

3.2. Structural characterization and electrochemical performance

The detailed structural information of HE-NLMNCMTO was then analyzed. The elemental composition determined by inductively coupled plasma atomic emission spectroscopy (ICP–AES) agrees well with the designed stoichiometry (Table S2), confirming the successful synthesis of the target composition. The crystal structure of HE-NLMNCMTO was investigated using X-ray diffraction (XRD) and Rietveld refinement. Fig. 2a shows the XRD pattern of HE-NLMNCMTO, which indicates an O3 type layered structure with a space group of $R\bar{3}m$. The sharp diffraction peaks of these HEOs suggest high crystallinity. The refined structural parameters (Table S3) further confirm the ordered arrangement of Na and transition-metal layers within the layered framework, as schematically illustrated in Fig. 2b. The morphology of the as-prepared HE-NLMNCMTO was observed using scanning electron microscopy (SEM), as shown in Fig. S17. Smooth flake-like particles with a size distribution in the range of ~2–4 μm demonstrated a typical layered structure. To probe the atomic-scale cation distribution, aberration-corrected high-angle annular dark-field scanning transmission electron microscopy (HAADF-STEM) was performed. The atomic-resolution image viewed along the [110] zone axis (Fig. 2c) exhibits irregular intensity variations within the transition-metal slabs, reflecting the random occupation of six different cations. The corresponding intensity profile further confirms the absence of elemental ordering, which is consistent with the characteristics of a high-entropy solid solution. In addition, the fast Fourier transform (FFT) pattern (Fig. S18) verifies the excellent crystallinity of the layered framework without detectable secondary phases. In addition, energy dispersive spectroscopy (EDS) elemental mapping (Fig. 2d) confirmed the homogeneous

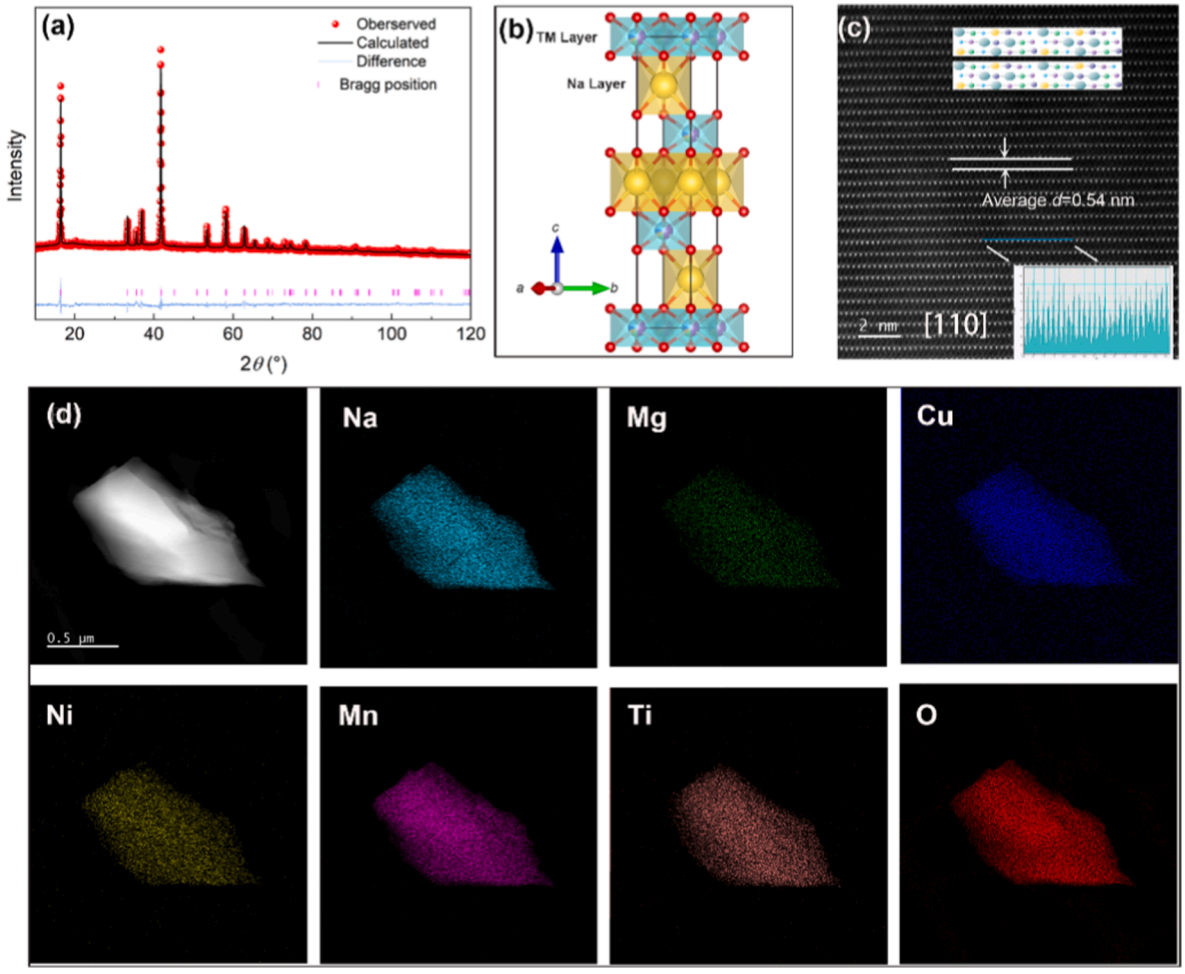


Fig. 2. Structural characterization of HE-NLMNCMTO sample. (a) Powder XRD pattern and Rietveld refinement of the as-synthesized HE-NLMNCMTO sample. (b) Schematic illustration of the O3 type structure showing the stacking sequence of the Na and TM layers. (c)HAADF-STEM image viewed along the [110] crystallographic direction and intensity profile according to the blue line (inset). (d) HRTEM image and EDS mapping for diverse elements in HE-NLMNCMTO.

distribution of the six elements in the prepared particles. X-ray absorption near-edge structure (XANES) analysis demonstrated that the oxidation states of Ni and Mn were approximately +2 and + 4, respectively, compared with standard references (Fig. S19). The local electronic structures of Cu^{2+}/Ni^{2+} were analyzed using extended X-ray absorption fine structure (EXAFS) spectroscopy. Fig. S20 shows the EXAFS spectra of Cu and Ni with the k^3-weighted $\chi(k)$ function. A relatively short Cu–O bond length (~1.5 Å) and a longer Ni–O bond length (~1.7 Å) can be calculated from the EXAFS spectra. However, the second shell M-Me for both spectra is located at approximately the same 2.5 Å, indicating that high-entropy effects lead to the random and even distribution of six metal ions in the TM layer [23].

The electrochemical properties of HE-NLMNCMTO were evaluated in Na half-cells within the voltage range of 2.0–4.2 V. As shown in Fig. 3a, the initial charge/discharge capacities were 195.8 mA·h/g and 167.1 mA·h/g with an initial coulombic efficiency of 85.3%. Specifically, The lower-voltage region below approximately 3.5 V is mainly associated with the oxidation of Ni^{2+} and Cu^{2+}, whereas the higher-voltage sloping region corresponds predominantly to oxygen-redox reactions. The latter contributes approximately 120 mA·h/g, indicating that lattice oxygen provides substantial additional charge compensation beyond the conventional transition-metal redox capacity. This indicates that oxygen redox provides ~60% of the total charge compensation, consistent with the DFT-predicted O 2p participation. The initial irreversible capacity

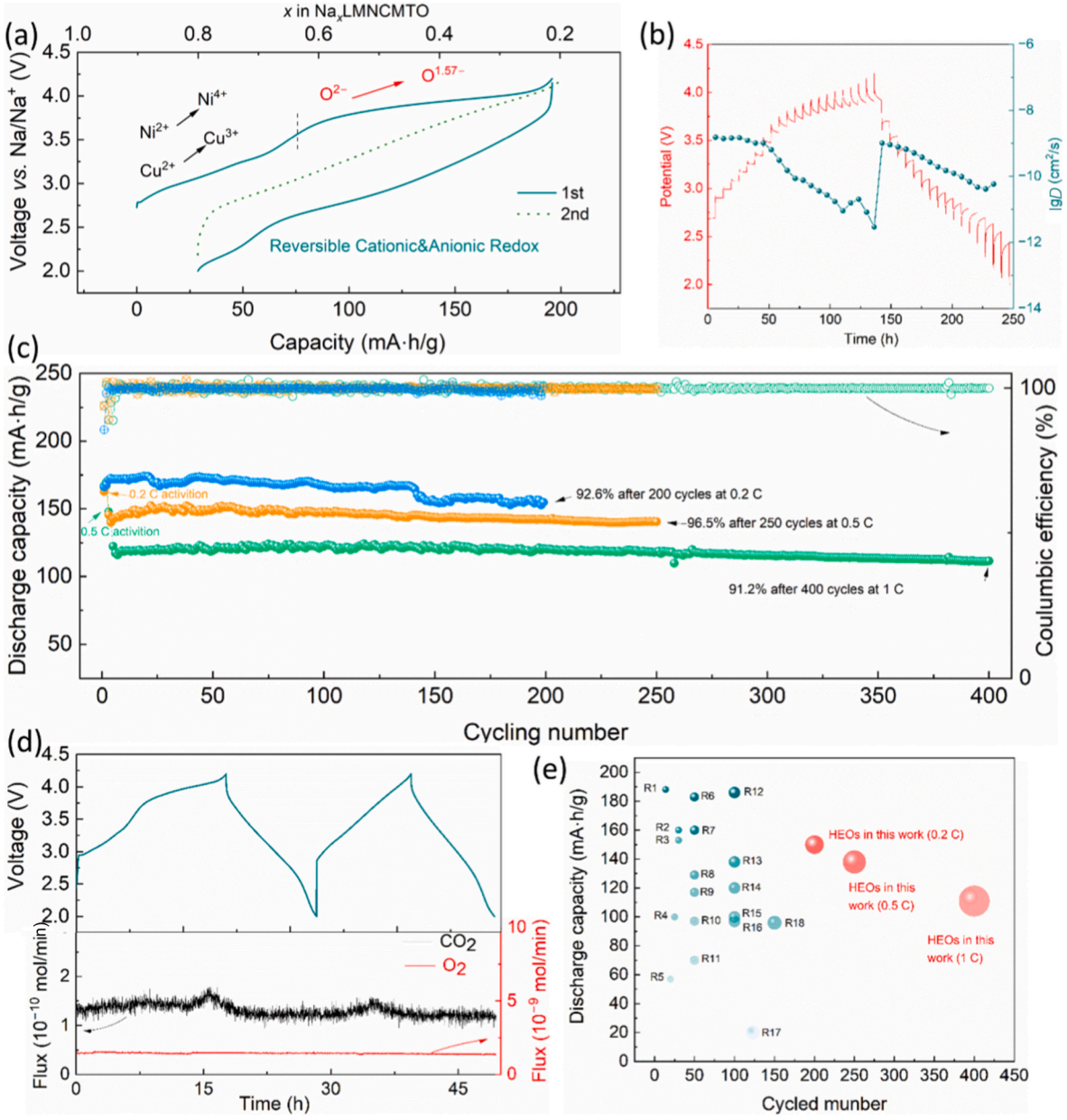


Fig. 3. Electrochemical performance of HE-NLMNCMTO cathode. (a) Typical charge/discharge profiles of the HE-NLMNCMTO cathode at a current rate of 0.2 C (1 C = 200 mA/g) in the voltage window of 2.0–4.2 V. (b) GITT curves and corresponding Na + apparent diffusion coefficients of NLMNCMTO during the charge and discharge processes. (c) Long-term cycling performance at 0.2/0.5/1.0 C with initial 2 cycles of the activation process. (d) DEMS data collected during the first two cycles. (e) Comparison of lifespan and retained capacity of reported oxide cathode materials with oxygen redox reaction for NIBs. (The diameter and transparency of the ball are directly proportional to its cycle life and specific capacity. Detailed information is presented in Table S4).

(14.7%) is predominantly associated with the non-fully reversible oxygen redox at the first cycle and a small amount of surface electrolyte decomposition, as supported by the differential electrochemical mass spectrometry (DEMS) and TOF-SIMS results. Notably, the subsequent cycles show negligible additional irreversibility, confirming that the HE structure stabilizes the oxygen redox after the initial activation. During the subsequent discharge process, the voltage profile evolves into a continuous slope. This electrochemical behavior can also be confirmed by the CV curves (Fig. S21). The two oxidation peaks that occurred in the first oxidation state agreed with the two-voltage platforms in the initial charge voltage profile, further confirming the reversible electrochemical behavior. The apparent Na^+ diffusion coefficient ($\sim 10^{-10}$ cm^2/s) was calculated using the galvanostatic intermittent titration technique (GITT), as shown in Fig. 3b. The OR of this HE-NLMNCMTO is completed below 4.2 V, substantially lower than that reported for most oxygen-redox layered oxides (>4.4 V), Operating within this moderate voltage window effectively suppresses electrolyte oxidation and irreversible structural degradation, providing a solid basis for achieving prolonged cycling stability.

Tailorable properties are the main driving factors for the increasing interest in HEOs. Coupled with the support of a greatly reduced charge cut-off voltage, long-term cycling stability may be the highlight of these HEOs electrode materials. Fig. 3c shows promising long-term cycling stability at a voltage range of 2.0–4.2 V at different current densities. Specifically, it shows an outstanding capacity retention of 92.6% after 200 cycles/96.5% after 250 cycles/91.2% after 400 cycles at 0.2, 0.5 C, and 1.0 C, respectively. All capacity retention values are calculated based on the discharge capacity after the second activation cycle. The material maintained a discharge capacity of 137.7 mA·h/g after 250 cycles, and almost no capacity decay was observed after 400 cycles at 1 C. In addition, the rate capability of HE-NLMNCMTO was evaluated between 2.0 and 4.2 V under various current densities from 0.05 C to 2.00 C, as shown in Fig. S22. The material still exhibited a capacity of ~120 mA·h/g at 2 C. The 2 C rate performance of HE-NLMNCMTO is competitive among O3-type oxygen-redox cathodes, yet there remains considerable room for improvement through further optimization of particle morphology, doping schemes, or electrode engineering. For example, the Al/Cu co-doped O3-$NaNi_{1/3}Fe_{1/3}Mn_{1/3}O_2$ (NFM) cathode delivers 113 mA·h/g at 5 C, while the Co-doped porous NFM cathode could achieves a better capability of 116.7 mA·h/g at 10 C report by Wen and co-workers [24,25]. The DEMS data collectively suggest that the HE-NLMNCMTO doesnot release O_2 gas, indicating a successful limitation for the over-oxidation leading to the catastrophic recombination of peroxo/superoxo species into gaseous O_2 gas (Fig. 3d). Trace CO_2 was observed originating from superficial electrolyte oxidation. The cycling performances and reversible capacity of the HE-NLMNCMTO cathode and other reported OR cathodes were compared, as shown in Fig. 3e. In which, the bubble diameter is proportional to the cycle number, and the transparency is inversely proportional to the remaining capacity (*i.e.*, darker bubbles indicate higher remaining capacity). All data are collected from reports with similar voltage windows and Na-metal counter electrodes to ensure a fair comparison. The detailed parameters are listed in Table S4. The proposed HE-NLMNCMTO exhibited the best cycling life and retained capacity at different current densities.

3.3. Charge compensation mechanism and structural stability analysis

The charge compensation of HE-NLMNCMTO during the charge/discharge process was investigated using hard/soft X-ray absorption spectroscopy (h/sXAS) and X-ray photoelectron spectroscopy (XPS). Fig. S23a–b displays the normalized XANES spectra of the Ni and Cu K-edges for various electrochemical states. As observed, the Ni K-edge and Cu K edge shifted to a higher energy when charged to 3.8 V, suggesting the oxidation of Ni^{2+} and Cu^{2+}. Notably, both the K-edges of Ni and Cu returned to low energy when charged further to 4.2 V. This may be associated with the reductive coupling mechanism or ligand-to-metal charge transfer (LMCT) process [26]. For the oxidation/reduction processes of Mn and O, soft X-ray absorption spectroscopy (sXAS) was performed, as shown in Fig. S24. The data were collected in total electron yield (TEY) mode, from which we obtained information with a detection depth of ~10 nm. The Mn spectra display two peaks in the high-energy range (metal L2-edge) and low-energy range (metal L3-edge), which are associated with the core-hole spin-orbital-coupling split [27]. The intensity ratios of the double-peak features in the Mn-L3 regions (A and B) have a negative relationship with the oxidation state of the TM. In the first charge and discharge process, the peak B Mn-L3 edge was relatively strong, indicating that Mn^{4+} was held in the bulk structure. When discharged to 2.0 V, the peak A Mn-L3 edge intensified, corresponding to the reduction of Mn^{4+} to Mn^{3+}.

The O K-edge sXAS in the high-energy range (above 535 eV) is attributed to excitation from the O 1s orbital to the hybridized orbital of TM and O. The pre-edge peak at a lower energy (531.4 eV) is related to the transition from the O 1s orbital to the unoccupied hybridized orbital of the TM 3d and O 2p [28]. As shown in Fig. S24b, the intensity of the pre-edge peak at 531.4 eV increased during the charging process, indicating an increase in the hole state. As Mn^{4+} is maintained in the charge process, as discussed above, it can be concluded that the increased hole state originates from O^{2-}. Notably, the intensified pre-edge is obvious at the first charge to 3.8 V, consistent with the theoretical prediction that HE construction lowers the electrochemical potential of oxygen redox.

High-entropy materials generally exhibit enhanced structural stability because of the synergistic effects arising from multiple constituent elements. To uncover the intrinsic mechanism of the excellent cycling stability of HE-NLMNCMTO, the combined *in-situ* XRD, nano computed tomography (nano-CT) and STEM were conducted. Fig. 4a and b shows the *in-situ* XRD patterns and the corresponding calculated evolution of the lattice volume. Pristine O3 evolves into O′3 when charging from OCV to 3.0 V, after which a new P3 phase emerges for further desodiation, and finally turns into an OP2 phase at the end of charging. Notably, the (003) reflection shifted to a higher angle at a high state of charge. This is caused by OR, which decreases the negative charge and has the opposite effect compared to the TM redox [29–31]. Notably, the phase transition was highly reversible compared to the XRD patterns for the first and the second charging processes. The lattice volume was calculated as shown in Fig. 4b. The lattice experienced a volume change of ~2.44%, indicating excellent structural stability during sodiation/desodiation. Fig. 4c shows the structural evolution during first cycle (the green and red arrows represent the charging and discharging processes). The 3D-reconstructed particle models of the nano-CT slices for HE-NLMNCMTO and non-HE-NLNMO before and after the cycles were conducted. As shown in Fig. 4d, the HE-NLMNCMTO particle maintains great particle integrity without any cracks even after 100 cycles, accounting for its outstanding cycling stability. However, non-HE-NLNMO showed obvious cracks (purple region) after cycling, and these cracks originated from the inside of the particle, which deteriorated the structural stability and consequently worsened the cycling life (Fig. S25). Besides, we tracked the evolution of the layered structure during the electrochemical cycling process using

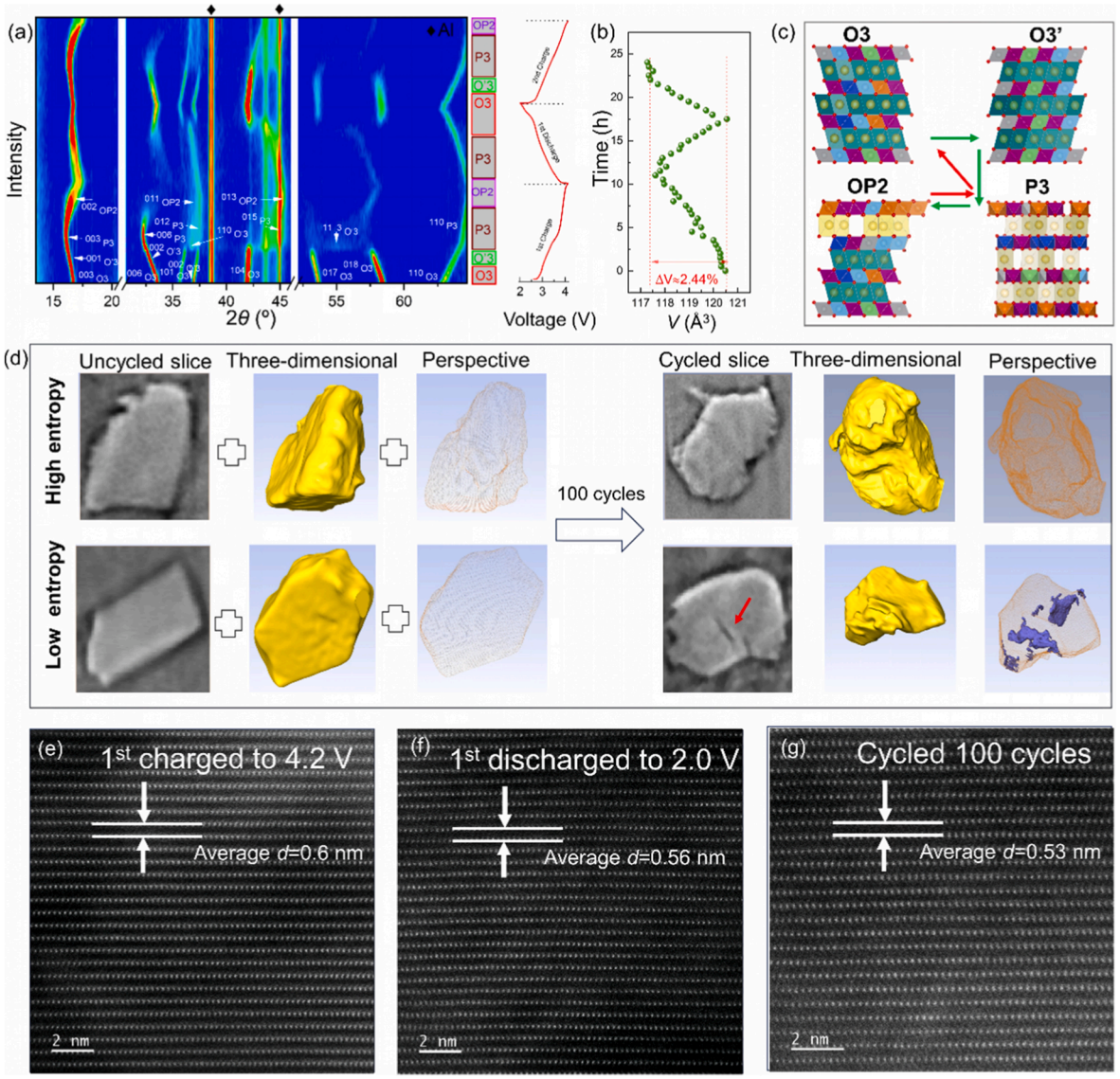


Fig. 4. Structural evolution of HE-NLMNCMTO in charge-discharge process. (a) *In-situ* XRD patterns and (b–c) calculated evolution of lattice volume and crystal structure evolution for HE-NLMNCMTO. (d) 3D-reconstructed particle model of nano-CT for HE-NLMNCMTO and non-HE-NLNMO cathode materials before and after 100 cycles; the purple region represents the cracks. (d-f) HAADF-STEM images of HE-NLMNCMTO at the first charge (4.2 V), first discharge (2.0 V) and 100-cycle-discharge (2.0 V) states. The detailed analysis process for interplanar spacing is shown in Fig. S26.

STEM analysis. Fig. 4e–g shows the HAADF images of HE-NLMNCMTO at the first charge (4.2 V), first discharge (2.0 V) and 100-cycle-discharge (2.0 V) states. Overall, the layered structure was well maintained with continuous charge and discharge, even after 100 cycles. When first charged to 4.2 V, the average interplanar (d) spacing of (003) increased to 0.6 nm owing to the increased repulsion of O–O in the deep desodiation state. The d-space decreased to 0.56 nm when the Na content recovered (discharge state), which is close to that of the as-prepared powders (0.54 nm in Fig. 2c). This observation indicates that the crystal structure can largely recover to its original state, demonstrating excellent structural reversibility. Even after 100 cycles, the average d-space was maintained at 0.53 nm, and the layered structure was well preserved, contributing to the excellent cycle life of this HE-NLMNCMTO. The Fast Fourier Transform (FFT), Inverse FFT and Intensity profile of HAADF-STEM images for HE- NLMNCMTO electrode at the status of 1st charged to 4.2 V, 1st discharged to 2.0 V and cycled after 100 cycles were shown in Fig. S26, respectively. These results also suggest a excellent structural stability of this HE- NLMNCMTO during the electrochemical process.

3.4. Behaviors of HEOR in Ah-level cells and anode-free pouch

To evaluate the practical applicability of the high-entropy oxygen-redox cathode beyond half-cell configurations. Firstly, the coin-type full cell consist of HE-NLMNCMTO//hard carbon (HC) was assembled and cycled between 1.0 and 4.2 V. The full cell exhibits a reversible specific capacity of 164.4 mAh/g (based on the cathode active mass) with an initial Coulombic efficiency of 78.2% at 0.1 C (Fig. 5a), confirming that the reversible oxygen-redox reaction can be effectively retained in practical full-cell configurations. Then, to further assess the scalability of the proposed material, kilogram-scale HE-NLMNCMTO powders were synthesized using the same solid-state process employed for laboratory-scale preparation. Ah-level cylindrical batteries coupled with hard carbon anode were successfully prepared, as seen the detailed

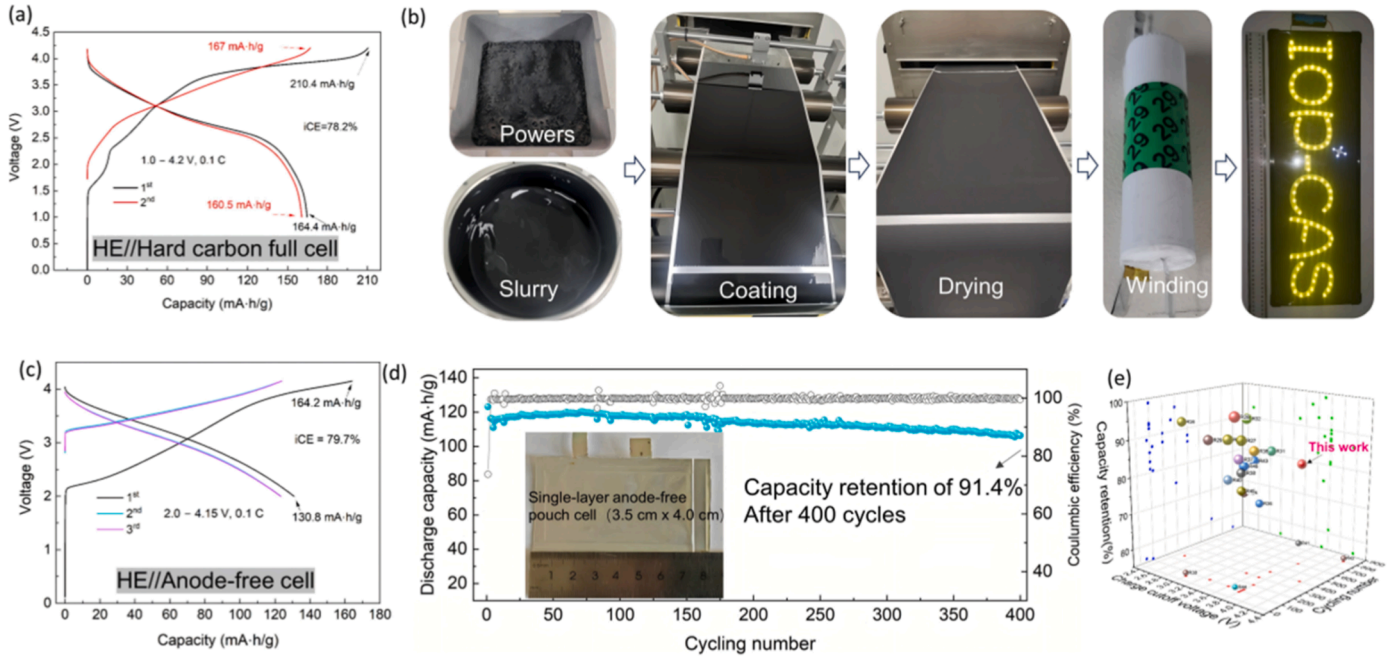


Fig. 5. Electrochemical performance of HE-NLMNCMTO in full cell and anode-free cell. (a) The charge-discharge curves of HE-NLMNCMTO -hard carbon(HC) full cell between 1.0 V and 4.2 V at 0.1 C. (b) The real photos of Ah-level cylindrical batteries preparing process and the lighted "IOP-CAS" powered by cylindrical batteries. (c) Charge-discharge curves of HE-NLMNCMTO -anode free cell between 2.0 V and 4.15 V at 0.1 C (the specific capacity is calculated based on the both mass of cathode and anode electrode). (d) Cycling performance of HE-NLMNCMTO in single-layer anode-free pouch cell at 0.5C. (e) Performance comparison of anode-free cell across the cycling number, charge cut-off voltage and capacity retention(the detail information is presented in Table S5).

processing procedure shown in Fig. 5b. Fig. S27 displays the galvanostatic charge and discharge profiles of prepared cylindrical batteries ranging from the first cycle to the 100th cycle, showing reversible voltage profiles and excellent cycling performance throughout prolonged operation. The lighted "IOP-CAS" shown indicates the promising practical application prospects of the proposed cathode in realistic battery systems.

Furthermore, to further challenge the structural stability of HE-NLMNCMTO under more demanding operating conditions, the single-layer anode-free pouch cell was also assembled and cycled between 2.0 and 4.15 V. As shown in Fig. 5c, this anode-free cell could display a reversible capacity of 130.8 mA·h/g (based on the total mass of cathode and anode electrode mass) with an initial Coulombic efficiency of 78.2% at 0.1 C. Benefiting from the high structural stability and suitable cutoff voltage window of HE-NLMNCMTO. This single-layer anode-free pouch cell maintains a high capacity retention of 91.4% after 400 cycles at 0.5 C (Fig. 5d), which outperform the other reported anode-free batteries across the cycling number, charge cut-off voltage and capacity retention (Fig. 5e).The ability to simultaneously achieve low-voltage oxygen-redox activation, long-term cycling stability, kilogram-scale synthesis, and successful demonstration in cylindrical and anode-free pouch cells highlights the considerable potential of the high-entropy strategy for the practical deployment of next-generation sodium-ion batteries.

4. Conclusion

In summary, conventional oxygen-redox cathodes generally suffer from poor cycling performance because of their intrinsic structural instability and the requirement for high charge cut-off voltages. Here, we demonstrate a high-entropy strategy for designing practical oxygen-redox cathodes. The high-entropy O3-type HE-NLMNCMTO delivers a high reversible capacity of 167.1 mA·h/g and outstanding cycling stability, retaining 91.2% of its capacity after 400 cycles at 1 C. The high-entropy configuration lowers the oxygen-redox potential and enables complete activation of oxygen redox below 4.2 V, thereby suppressing electrolyte decomposition and irreversible structural degradation. Combined with its intrinsically stable framework, HE-NLMNCMTO exhibits excellent performance in both cylindrical cells and anode-free pouch cells, demonstrating considerable potential for practical sodium-ion batteries. This work provides a promising strategy for developing durable oxygen-redox cathodes with practical applicability.

CRediT authorship contribution statement

Rongbin Dang: Writing – review & editing, Writing – original draft, Visualization, Resources, Investigation, Funding acquisition, Formal analysis, Conceptualization. **Rui Gao:** Visualization, Investigation. **Weiliang Xu:** Investigation. **Xiaohui Rong:** Writing – review & editing, Investigation. **Dongdong Xiao:** Investigation, Formal analysis. **Feixiang Ding:** Formal analysis. **Lin Zhou:** Investigation. **Huican Mao:** Writing – original draft, Software, Investigation. **Yaxiang Lu:** Resources. **Junmei Zhao:** Writing – original draft, Resources, Investigation. **Meicheng Li:** Writing – review & editing, Supervision, Resources. **Yong-Sheng Hu:** Writing – review & editing, Supervision, Project administration, Funding acquisition, Conceptualization.

Declaration of competing interest

The authors declare that they have no known competing financial interests or personal relationships that could have appeared to influence the work reported in this paper.

Acknowledgement

This work was financially supported by the following foundations: the National Natural Science Foundation (NSFC) of China

(52394170, 52394174, 52202333, 92372116, and 22422906); the Commanding Heights of Science and Technology of Chinese Academy of Sciences (LDES15 0000); the Fundamental Research Funds for the Central Universities (2026MS048); China Postdoctoral Science Foundation founded Project (2022M713337); the Beijing Natural Science Foundation (JQ24006); Young Elite Scientists Sponsorship Program by CAST (2022QNRC001). International Cooperation and Exchange (52561160145), Beijing Natural Science Foundation (26JL002). We thank the 1W1B-XAFS Beamline of Beijing Synchrotron Radiation Facility (https://cstr.cn/31109.02.BSRF.1W1B) for providing technical support and assistance in XAFS data collection and Allocation of beamtime at 4W1A (31109.02.BSRF.4W1A) is gratefully acknowledged.

Appendix A. Supplementary data

Supplementary data to this article can be found online at https://doi.org/10.1016/j.jmat.2026.101326.

References

[1] Hu Y-S, Lu Y. Nobel prize for the Li-ion batteries and new opportunities and challenges in Na-ion batteries. ACS Energy Lett 2019;4(2019):2689–90.
[2] Liu L, Mo J, Li J, Liu J, Yan H, Lyu J, et al. Comprehensively-modified polymer electrolyte membranes with multifunctional PMIA for highly-stable all-solid-state lithium-ion batteries. Nano Energy 2020;48:334–43.
[3] Zhao C, Wang Q, Yao Z, Wang J, Sánchez-Lengeling B, Ding F, et al. Rational design of layered oxide materials for sodium-ion batteries. Science 2020;370:708–11.
[4] Pan H, Hu Y-S, Chen L. Room-temperature stationary sodium-ion batteries for large-scale electric energy storage. Energy Environ Science 2013;6:2338–60.
[5] Hwang J-Y, Myung S-T, Sun Y-K. Sodium-ion batteries: present and future. Chem Soc Rev 2017;46:3529–614.
[6] Xiang X, Zhang K, Chen J. Recent advances and prospects of cathode materials for sodium-ion batteries. Adv Mater 2015;27:5343–64.
[7] Fang C, Huang Y, Zhang W, Han J, Deng Z, Cao Y, et al. Routes to high energy cathodes of sodium-ion batteries. Adv Energy Mater 2016;6:1501727.
[8] Han MH, Gonzalo E, Singh G, Rojo T. A comprehensive review of sodium layered oxides: powerful cathodes for Na-ion batteries. Energy Environ Sci 2015;8:81–102.
[9] He W, Guo W, Wu H, Lin L, Liu Q, Han X, et al. Challenges and recent advances in high capacity Li-rich cathode materials for high energy density lithium-ion batteries. Adv Mater 2021;33:2005937.
[10] Jiang B, Li J, Luo B, Yan Q, Li H, Liu L, et al. $LiPO_2F_2$ electrolyte additive for high-performance Li-rich cathode material. J Energy Chem 2021;60:564–71.
[11] Rong X, Hu E, Lu Y, Meng F, Zhao C, Wang X, et al. Anionic redox reaction-induced high-capacity and low-strain cathode with suppressed phase transition. Joule 2019;3:503–17.
[12] Wang Q, Mariyappan S, Rousse G, Morozov AV, Porcheron B, Dedryvère R, et al. Unlocking anionic redox activity in O3-type sodium 3d layered oxides via Li substitution. Nat Mater 2021;20:353–61.
[13] Ren H, Li Y, Ni Q, Bai Y, Zhao H, Wu C. Unraveling anionic redox for sodium layered oxide cathodes: breakthroughs and perspectives. Adv Mater 2022;34:2106171.
[14] Jin J, Liu Y, Pang X, Wang Y, Xing X, Chen J. A comprehensive understanding of the anionic redox chemistry in layered oxide cathodes for sodium-ion batteries. Sci China Chem 2021;64:385–402.
[15] Park JH, Ko IH, Lee J, Park S, Kim D, Yu SH, et al. Anionic redox reactions in cathodes for sodium-ion batteries. Chemelectrochem 2021;8:625–43.
[16] Gao H, Li J, Zhang F, Li C, Xiao J, Nie X, et al. Revealing the potential and challenges of high-entropy layered cathodes for sodium-based energy storage. Adv Energy Mater 2024;14:2304529.
[17] Duan L, Zhang Y, Tang H, Liao J, Zhou G, Zhou X. Recent advances in high-entropy layered oxide cathode materials for alkali metal-ion batteries. Adv Mater 2025;37:2411426.
[18] Zhao C, Ding F, Lu Y, Chen L, Hu Y-S. High-entropy layered oxide cathodes for sodium-ion batteries. Angew Chem Int Ed 2020;59:264–9.
[19] Ding F, Zhao C, Xiao D, Rong X, Wang H, Li Y, et al. Using high-entropy configuration strategy to design Na-ion layered oxide cathodes with superior electrochemical performance and thermal stability. J Am Chem Soc 2022;144:8286–95.
[20] Ding F, Ji P, Han Z, Hou X, Yang Y, Hu Z, et al. Tailoring planar strain for robust structural stability in high-entropy layered sodium oxide cathode materials. Nat Energy 2024;9:1529–39.
[21] Fu F, Liu X, Fu X, Chen H, Huang L, Fan J, et al. Entropy and crystal-facet modulation of P2-type layered cathodes for long-lasting sodium-based batteries. Nat Commun 2022;13:2826.
[22] Vaidya M, Muralikrishna GM, Murty BS. High-entropy alloys by mechanical alloying: a review. J Mater Res 2019;34:664–86.
[23] Lin C-C, Liu H-Y, Kang J-W, Yang C-C, Li C-H, Chen H-YT, et al. *In-situ* X-ray studies of high-entropy layered oxide cathode for sodium-ion batteries. Energy Storage Mater 2022;51:159–71.
[24] Lu H, Dai Z, Wen J, Feng S, Xiong P, Chen H, et al. Dual engineering of porosity and Co-doping enables ultrafast and stable $NaNi_{1/3}Fe_{1/3}Mn_{1/3}O_2$ cathodes for sodium-ion batteries. Mater Today 2026;98:103408.
[25] Feng S, Zheng C, Song Z, Wu X, Wu M, Xu F, et al. Boosting fast ionic transport and stability of O3-$NaNi_{1/3}Fe_{1/3}Mn_{1/3}O_2$ cathode via Al/Cu synergistically modulating microstructure for high-rate sodium-ion batteries. Chem Eng J 2023;475:146090.
[26] Li B, Tarascon J-M. 7.02 - status of Li(Na)-based anionic redox materials for better batteries. In: Reedijk J, Poeppelmeier KR, editors. Comprehensive inorganic chemistry III. third ed. Oxford: Elsevier; 2023. p. 6–45.
[27] Ding F, Meng Q, Yu P, Wang H, Niu Y, Li Y, et al. Additive-free self-presodiation strategy for high-performance Na-ion batteries. Adv Funct Mater 2021;31:2101475.
[28] Hu B, Geng F, Zhao C, Doumert B, Trebosc J, Lafon O, et al. Deciphering the origin of high electrochemical performance in a novel Ti-substituted P2/O3 biphasic cathode for sodium-ion batteries. ACS Appl Mater Interfaces 2020;12:41485–94.
[29] Hirsh H, Li Y, Cheng J-H, Shimizu R, Zhang M, Zhao E, et al. The negative impact of transition metal migration on oxygen redox activity of layered cathode materials for Na-ion batteries. J Electrochem Soc 2021;168:040539.
[30] Xu H, Guo S, Zhou H. Review on anionic redox in sodium-ion batteries. J Mater Chem A 2019;7:23662–78.
[31] Voronina N, Yaqoob N, Kim HJ, Lee K-S, Lim H-D, Jung H-G, et al. A new approach to stable cationic and anionic redox activity in O3-layered cathode for sodium-ion batteries. Adv Energy Mater 2021;11:2100901.